Supplementary A – Photographs of experimental apparatus

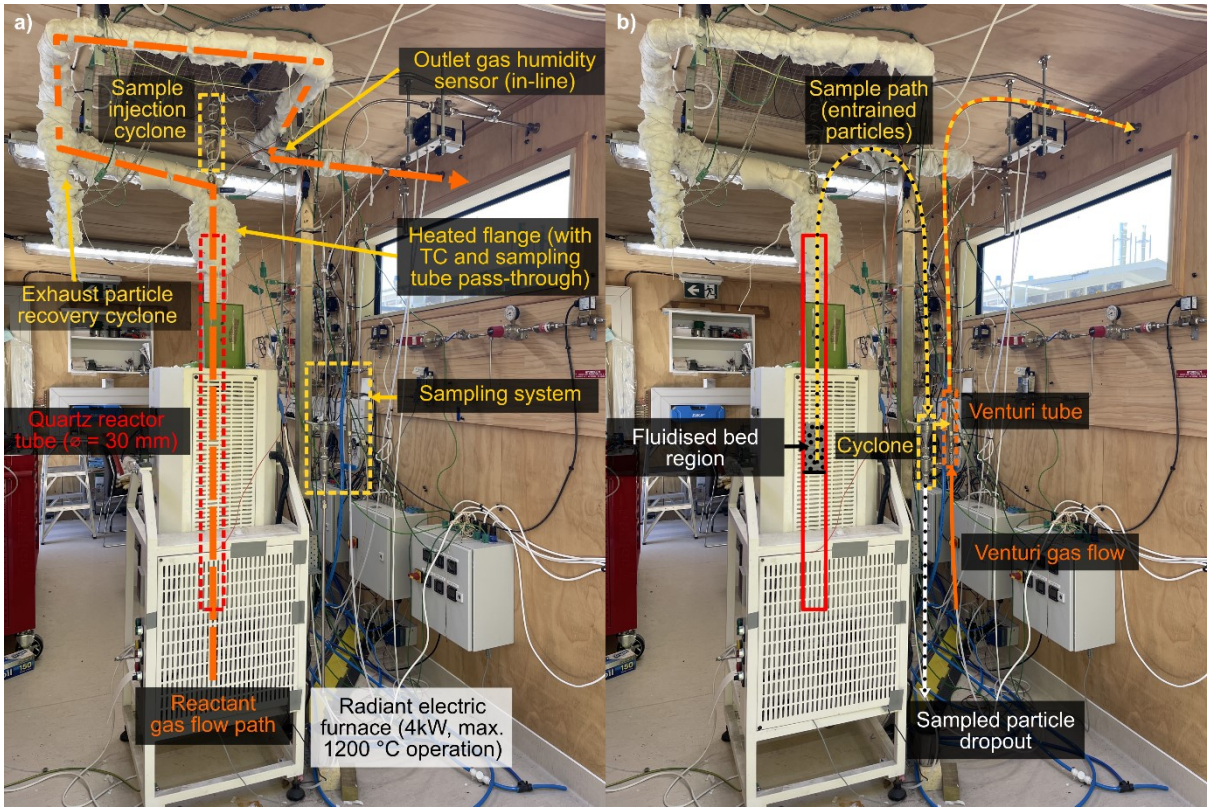

Figure A.1 – Photograph of the fluidised bed reactor assembly used for hydrogen reduction experiments, with: a) the location of key components and the primary reactant gas flow path are labelled; b) the key components of the sample recovery system labelled, wherein a venturi tube generates a negative pressure to draw fluidised particles into a cyclone for recovery.

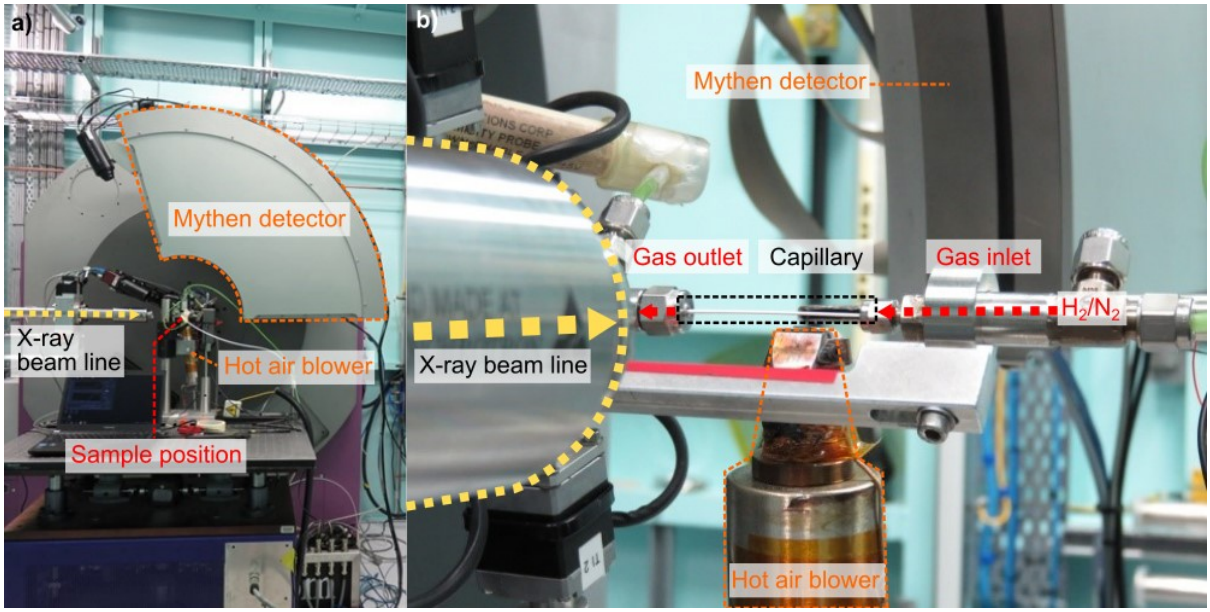

Figure A.2 – Photographs of the high-temperature synchrotron apparatus viewed a) parallel to the bore of the sample capillary and b) across the sample capillary, along the X-ray beam line.

Supplementary B – Parameters for TOPAS fitting

Global parameters used for fitting of data in Topas 4.2 are as follows:

- Background: Chebychev (6 parameters, fitted)
- Zero error (fitted)
- Lorentz polarisation: 90°
- Capillary diameter: 0.5 mm
- Capillary μ: 50 cm^{-1}
- Convolutions:
    - Gauss, 1/Cosθ, 0.00754
    - Circles, Sin(2θ), 0.07042
    - Hat, Tanθ, 0.04154
- Wavelength: 0.58891 Å

These were fixed according to values obtained from fitting a LaB_6 standard.

For the structural models of each crystalline phase, the temperature factor Beq is defined for each atomic species. BeqFe was fitted, with BeqO fixed using the average of the first 10 scans at temperature before the reaction began. BeqTi was defined as 0.8*BeqFe + 0.2*BeqO. Structural models used for each phase are defined below (*: fitted parameter; L: Lorentzian; G: Gaussian). A list of sources for each model are given at the end of this appendix.

Hematite, $R\bar{3}c$
Fe_2O_3
Ref. B1

Atom	x	y	z
Fe	0	0	0.3553
O	0.3059	0	0.25

	TTM	MAG
a [Å]	5.113*	5.092*
c [Å]	13.960*	13.861*
Crystallite size	G*	L*, G*
Strain	L*	L*

Magnetite, $Fd\bar{3}m$
Fe_3O_4
Ref. B2
(Ti only occupies octahedral sites, Ref. B3)

Atom	x	y	z
$Fe_{0.8}Ti_{0.2}$	0.125	0.125	0.125
Fe	0.5	0.5	0.5
O	0.2548	0.2548	0.2548

	TTM.	MAG
a [Å]	8.49* 8.54* 8.58*	8.501*
Crystallite size	G*	L*, G*
Strain	L*, G*	L*

Wüstite, $Fm\bar{3}m$
FeO
Ref. B4

Atom	x	y	z
Fe	0	0	0
O	0	0	0.5

	TTM	MAG
a [Å]	4.355*	4.347*
Crystallite size	G	G*
Strain	L, G	L*, G*

Austenite, $Fm\bar{3}m$
Fe (fcc)
Ref. B5

Atom	x	y	z
Fe	0	0	0

	TTM	MAG
a [Å]	3.6440*	3.6454*
Crystallite size	G*	G*
Strain	L*, G*	L*, G*

Ferrite, $Im\bar{3}m$
Fe (bcc)
Ref. B6

Atom	x	y	z
Fe	0	0	0

	TTM	MAG
a [Å]	2.9028*	2.9033*
Crystallite size	G*	G*
Strain	L*, G*	L*

Ilmenite, $R\bar{3}$
$FeTiO_3$
Ref. B7

Atom	x	y	z
Fe	0	0	0.3569
Ti	0	0	0.1472
O	0.3192	0.025	0.245

	TTM
a [Å]	5.127*
c [Å]	14.16*
Crystallite size	G*
Strain	L*, G*

Rutile, $P4_2/mnm$
TiO_2
Ref. B8

Atom	x	y	z
Ti	0	0	0
O	0.3056	0.3056	0

	TTM
a [Å]	4.631*
c [Å]	2.985*
Crystallite size	G*
Strain	-

B1. R. L. Blake, R. E. Hessevick, T. Zoltai and L. W. Finger, 'Refinement of the hematite structure', Amer. Mineral. 51 (1966) 123-129.

B2. W. C. Hamilton, 'Neutron diffraction investigation of the 119°K transition in magnetite', Phys. Rev. 110 (1958) 1050-1057.

B3. B. A. Wechsler, D. H. Lindsley and C. T. Prewitt, 'Crystal structure and cation distribution in titanomagnetites ($Fe_{(3-x)}Ti_xO_4$)', Amer. Mineral. 69 (1984) 754-770.

B4. B. Hentschel, 'Stoichiometric FeO as metastable intermediate of the decomposition of wustite at 225°C', Z. Naturforsch. A 25 (1970) 1996-1997.

B5. R. Kohlhaas, P. Dunner and N. Schmitz-Pranghe, 'Uber die temperaturabhangigkeit der gitterparameter von eisen, kobalt und nickel im bereich hoher temperaturen', Z. Angew. Phys. 23 (1967) 245-249.

B6. H. E. Swanson, R. K. Fuyat and G. M. Ugrinic, 'Standard X-ray diffraction powder patterns: Alpha-iron (cubic)', Nat. Bur. Stand. (US) Circ. 539 (1955) 3.

B7. B. A. Wechsler and C. T. Prewitt, 'Crystal structure of ilmenite ($FeTiO_3$) at high temperature and at high pressure', Amer. Mineral. 69 (1984) 176-185.

B8. K. Sugiyama and Y. Takeuchi, 'The crystal structure of rutile as a function of temperature up to 1600°C', Z. Kristallogr. 194 (1991) 305-313.

Supplementary C – SEM and EDS maps of fluidised bed reduced particles

Additional electron microscopy images are presented below, providing further context for the microstructural evolution of TTM during hydrogen reduction. All of the samples shown were produced from fluidised bed reduction of unmilled TTM at 938 °C.

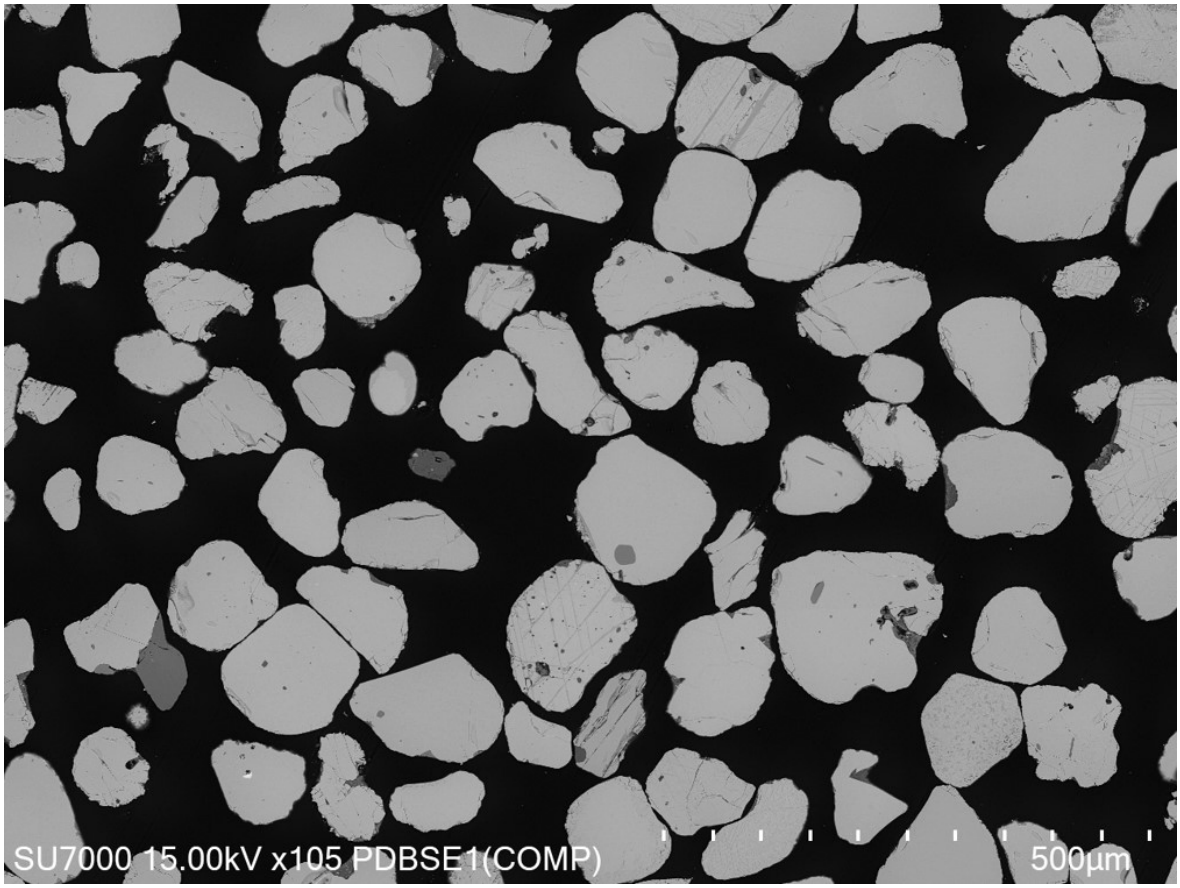

Figure C.1 – Low magnification image of unreduced TTM particles. Several particles featuring hematite lamellae – visible as dark parallel laths – are present.

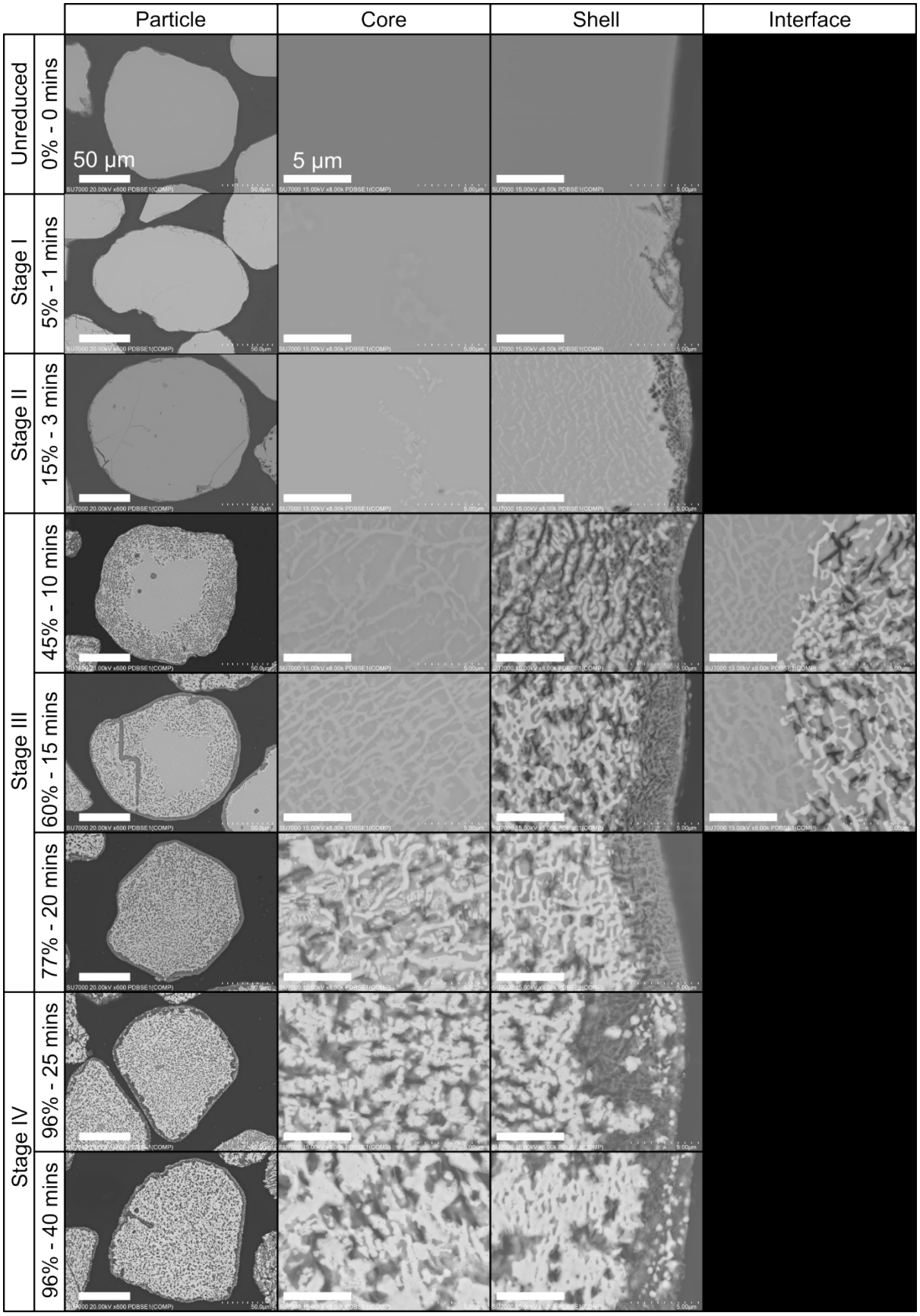

Figure C.2 – SEM micrographs of representative TTM particles sampled from fluidised bed reduction experiment. All low magnification image (Particle) scale bars 50 µm, all high magnification image (Core/Shell/Interface) scale bars 5 µm.

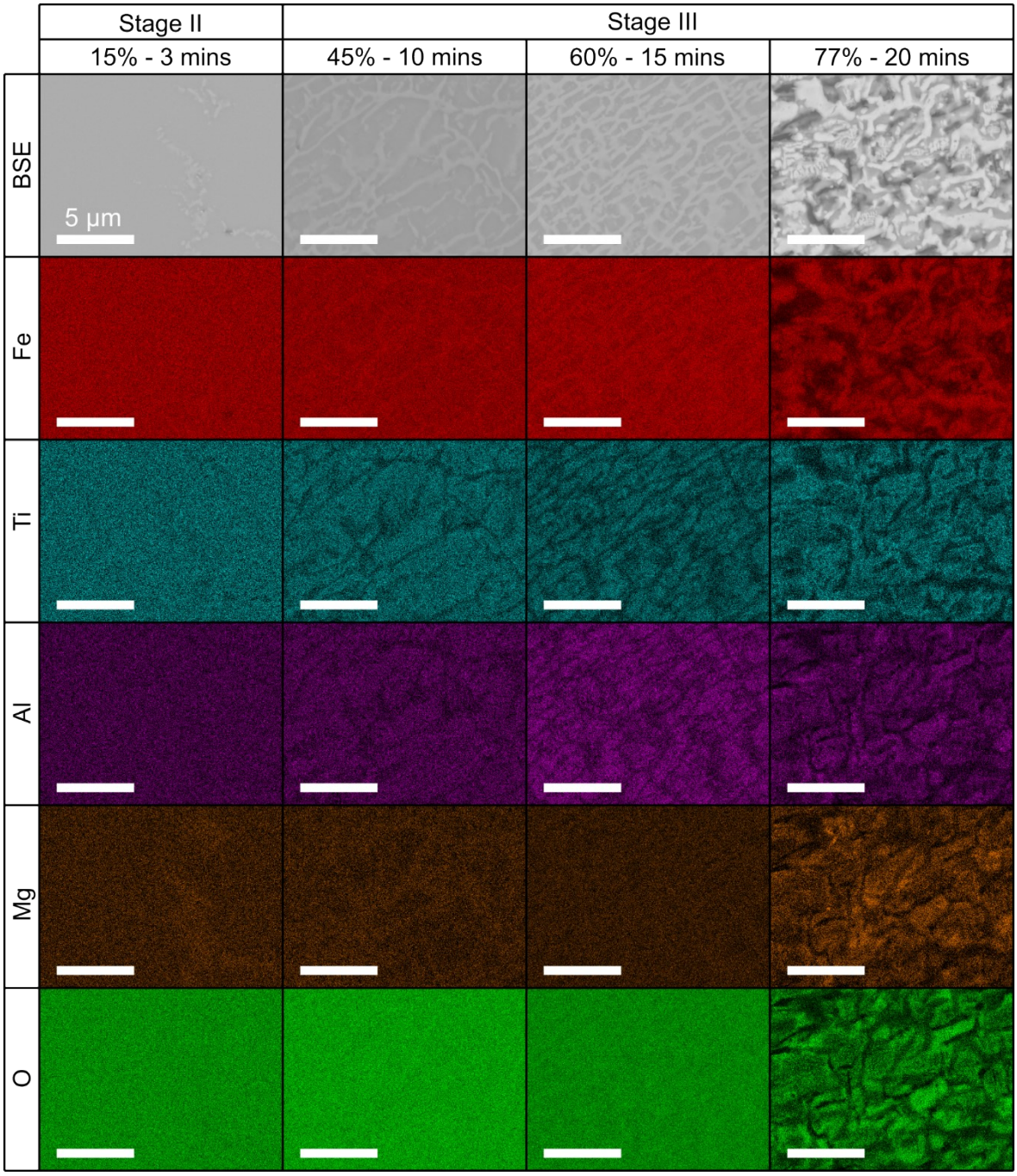

Figure C.3 – Microstructural evolution and EDS maps of the centre of representative TTM particles sampled from fluidised bed reduction. The degree of reduction and timepoint of sampling is given. All scale bars are 5 µm.

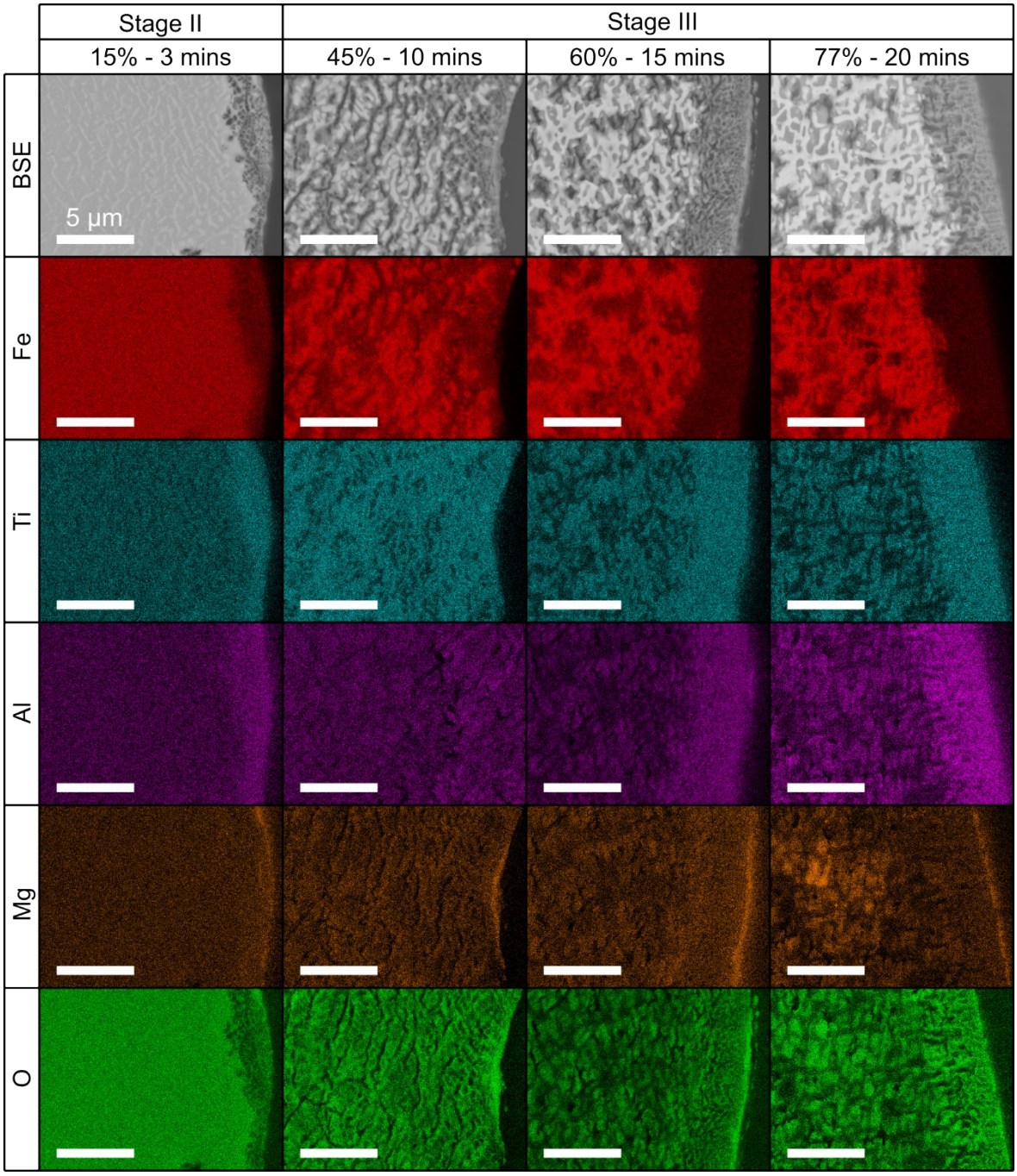

Figure C.4 – Microstructural evolution and EDS maps of the outer edge of representative TTM particles sampled from fluidised bed reduction. The degree of reduction and timepoint of sampling is given. All scale bars are 5 µm.

Supplementary D – Reported data for compositional and thermal dependence of lattice parameters

Table D.1 – Summary of key reference data on the compositional and temperature dependency of lattice parameters in the Fe-M-O ternary system for relevant metal dopants (Ti, Mg, Al).

Structure	Formula	Variable	Range	Comment	Source
Hematite /ilmenite ($R\bar{3}/R\bar{3}c$)	$Fe_{(2-x)}Ti_xO_3$	Ti/(Ti+Fe)	0 – 0.5 ($0 < x < 1$)	Increases with *x*.	[1]
	$Fe_{(2-x)}Mg_xO_3$	Mg/(Mg+Fe)	0.1 ($x = 0.2$)	Increases with *x*.	[2]
	$Fe_{(2-x)}Al_xO_3$	Al/(Al+Fe)	0 – 0.12 ($0 < x < 0.24$)	Decreases with *x*.	[3]
	Fe_2O_3	Temperature	25 – 755 °C	Non-linearity around the Néel temperature, and above cation ordering temp in solid solution.	[4]
	$FeTiO_3$	Temperature	24 – 1050 °C		[5–7]
Inverse spinel/ spinel ($Fd\bar{3}m$/ $F\bar{4}3m$)	$Fe_{(3-x)}Ti_xO_4$	Ti/(Ti+Fe) Ti/(Ti+Fe) Temperature	0 – 0.31 ($0 < x < 0.94$) 0 – 0.33 ($0 < x < 1$) 200 – 700 °C	Increases with *x*. Increases with *x* and T, remains approximately linear.	[8] [9]
	$Fe_{(3-x)}Mg_xO_4$	Mg/(Mg+Fe)	0.33 ($x = 1$)	Dependent upon degree of cation ordering	[10]
	$Fe_{(3-x)}Al_xO_4$	Al/(Al+Fe)	0 – 0.17 ($0 < x < 0.5$)	Within magnetite solid solution regime	[11]
	Fe_3O_4	Temperature	25 – 1000 °C	Dependency on oxygen fugacity	[12–14]
	$Fe_{(3-x)}O_4$	Fe:O ratio	$0 < x < 0.33$	Decreases with *x*. May transition to γ-Fe_2O_3.	[15]
Wüstite ($Fm\bar{3}m$)	Fe_xO	Fe:O ratio	$0.89 < x < 1$	Increases with *x*.	[16]
Austenite ($Fm\bar{3}m$)	Fe-γ	Temperature	910 – 1277 °C	Increases with T.	[17]
Ferrite ($Im\bar{3}m$)	Fe-α	Temperature	22 – 910 °C	No data for α-stabilised material above 910 °C	[17]
Pseudo-brookite (Bbmm)	$Fe_{(2-x)}Ti_{(1+x)}O_5$	Ti/(Ti+Fe)	0 – 0.5 ($0 < x < 1.0$)	Increases with *x*. Significant non-linearity in a axis.	[18]
Rutile (P42/mnm)	TiO_2	Temperature	25 – 996 °C	Increases with T.	[19]

D1 N. E. Brown, A. Navrotsky, G. L. Nord and S. K. Banerjee, *American Mineralogist*, 1993, **78**, 941–951.

D2 F. J. Berry, C. Greaves, Ö. Helgason, J. McManus, H. M. Palmer and R. T. Williams, *J. Solid State Chem.*, 2000, **151**, 157–162.

D3 J. Majzlan, A. Navrotsky and B. J. Evans, *Phys. Chem. Miner.*, 2002, **29**, 515–526.

D4 P. Fabrykiewicz, M. Stękiel, I. Sosnowska and R. Przeniosło, *Acta Crystallogr. B Struct. Sci. Cryst. Eng. Mater.*, 2017, **73**, 27–32.

D5 B. A. Wechsler and C. T. Prewitt, *American Mineralogist*, 1984, **69**, 176–185.

D6 J. Song, D. Fan, S. Huang, S. Zhang, M. Wu, W. Chen and W. Zhou, *Acta Geochimica*, 2023, **42**, 988–997.

D7 R. J. Harrison and S. A. T. Redfern, *Phys. Chem. Miner.*, 2001, **28**, 399–412.

D8 C. I. Pearce, C. M. B. Henderson, N. D. Telling, R. A. D. Pattrick, J. M. Charnock, V. S. Coker, E. Arenholz, F. Tuna and G. van der Laan, *American Mineralogist*, 2010, **95**, 425–439.

D9 Y. HAMANO, *Journal of geomagnetism and geoelectricity*, 1989, **41**, 65–75.

D10 C. Melai, T. Boffa Ballaran, L. Uenver-Thiele, A. Kurnosov, A. I. Chumakov, D. Bessas and D. J. Frost, *Phys. Chem. Miner.*, DOI:10.1007/s00269-022-01217-2.

D11 Y. Kapelyushin, Y. Sasaki, J. Zhang, S. Jeong and O. Ostrovski, *Metallurgical and Materials Transactions B*, 2015, **46**, 2564–2572.

D12 G. R. Holcomb, *Materials at High Temperatures*, 2019, **36**, 232–239.

D13 D. Levy, G. Artioli and M. Dapiaggi, *J. Solid State Chem.*, 2004, **177**, 1713–1716.

D14 D. Levy, R. Giustetto and A. Hoser, *Phys. Chem. Miner.*, 2012, **39**, 169–176.

D15 I. Kinebuchi and A. Kyono, *Journal of Mineralogical and Petrological Sciences*, 2021, **116**, 211–219.

D16 C. A. McCammon and L. Liu, *Phys. Chem. Miner.*, 1984, **10**, 106–113.

D17 I. Seki and K. Nagata, *ISIJ International*, 2005, **45**, 1789–1794.

D18 W. Q. Guo, S. Malus, D. H. Ryan and Z. Altounian, *Journal of Physics: Condensed Matter*, 1999, **11**, 6337–6346.

D19 D. Y. Chung, P. J. Heaney, J. E. Post, J. E. Stubbs and P. J. Eng, *Journal of Physics and Chemistry of Solids*, 2023, **177**, 111284.

Supplementary E – Comparison of in-situ synchrotron and fluidised bed XRD

Plotting of patterns against sin(θ)/λ allows comparison of data from different X-ray sources, noting that different source contributions will play a role in peak shape and background intensity. Peaks are observed at lower sin(θ)/λ ratio for synchrotron measurements due to the elevated temperature

Good correlation in the diffraction peaks present and the trend in intensity with reduction degree is observed (*Figure E.1*a). The presence of Fe-γ and ilmenite versus rutile and pseudobrookite are the only significant differences observed in behaviour over this range.

Asymmetry of the inverse spinel diffraction peaks is observed in both experiments (*Figure E.1*b).

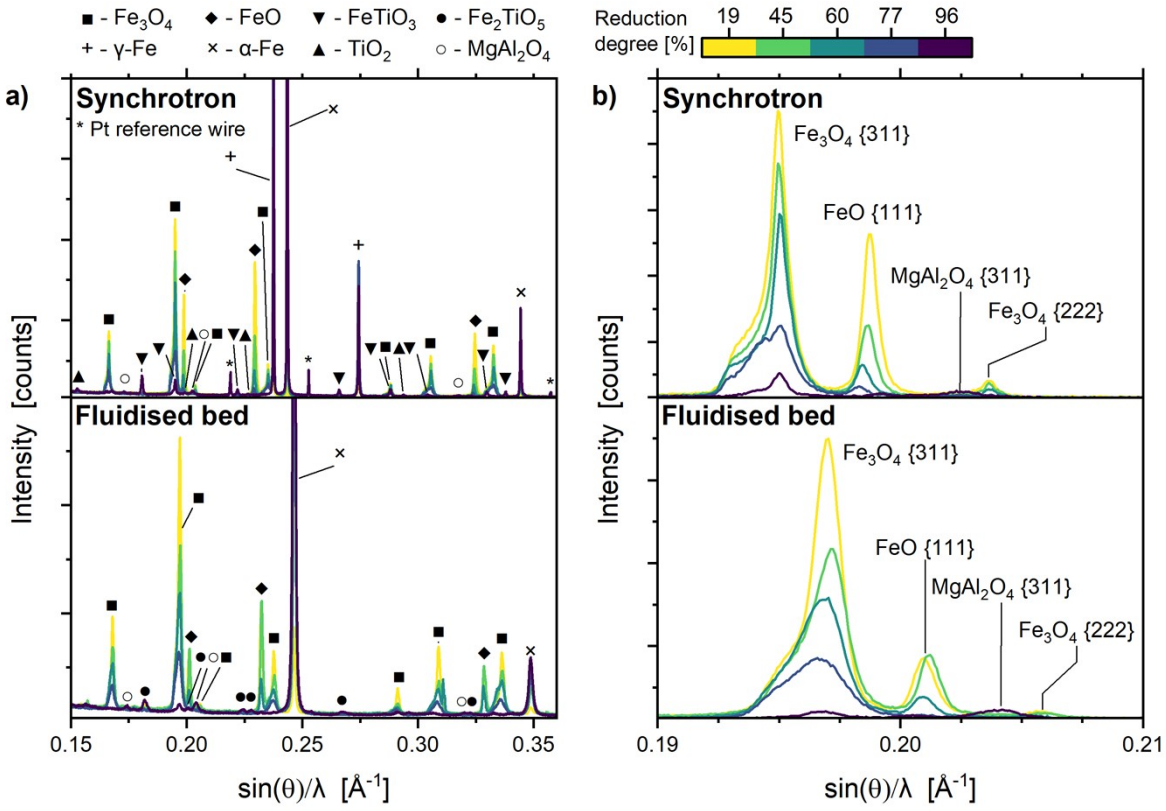

Figure E.1 – a) Comparison of diffraction patterns with matched degree of reduction for in-situ synchrotron measurements, and ex-situ partially reduced fluidised bed samples of TTM. b) Comparison of selected diffraction pattern peaks for in-situ synchrotron and fluidised bed samples of TTM, indicating similar asymmetry of the inverse spinel peaks.

Supplementary F – Calculation of theoretical equilibrium phases

Calculations performed in FactSage v8.2 using the FactPS, FToxid and FSstel databases with pure liquids enabled. Where multiple reference states were available, the phase with the highest activity was selected.

Table F.1 – Predicted composition of stable phases for TTM.

Phase	Mass fraction (%)	Elemental composition (at%) / Activity									
		Fe	Mn	V	Ti	Ca	P	Si	Al	Mg	O
FCC_A1#1	62.51	99.97	1E-04	1E-06	1E-12	2E-21	3E-02	1E-07	9E-11	5E-15	2E-08
Titania_Spinel	28.69	20.21	7E-01		1E+01				2.78	6.19	57.14
V_Spinel	5.09	11.33		4.05					23.67	3.81	57.14
Olivine#1	2.94	15.32	2.92			2E-01		14.29		10.14	57.14
Spinel#1	0.51	10.13	5E-01						28.36	3.82	57.14
Slag-liq#1	0.26	3E-03	2E-01	2E-03	3.48	17.98	12.31	3.32	3E-03	0.96	61.76

Table F.2 – Predicted composition of stable phases for TTM..

Phase	Mass fraction (%)	Elemental composition (at%) / Activity									
		Fe	Mn	V	Ti	Ca	P	Si	Al	Mg	O
FCC_A1#1	97.64	100.00	3E-04	3E-06	7E-13	2E-20	2E-03	5E-08	6E-11	1E-14	2E-08
Titania_Spinel	1.13	18.10	1.18	13.56					2E+00	8E+00	57.14
V_Spinel	0.78	10.82	10.51						16.48	5.04	57.14
Olivine#1	0.39	10.43	3.89			1.16		14.29		13.10	57.14
Slag-liq#1	0.06	9E-04	9E-02	5E-03	3.08	19.24	12.09	3.44	3E-03	5E-01	61.56

Table F.3 – Activity and calculated activity coefficients of species in predicted end-phase austenite for TTM.

Species	austenite composition (FCC_A1#1) wt %	activity	reference phase	activity coefficient
Al	4.11E-11	4.07E-16	Al_liquid	9.90E-04
Ca	1.76E-21	4.50E-18	Ca_liquid	2.55E+05
Fe	99.982	0.99968	Fe_FCC_A1	1.00E+00
Mg	2.31E-15	6.69E-14	Mg_liquid	2.90E+03
Mn	1.33E-04	9.99E-07	Mn_cub_A13	7.49E-01
O	4.61E-09	1.01E-17	O2(g)	2.19E-07
P	1.78E-02	1.12E-08	P_liquid	6.29E-05
Si	5.44E-08	3.43E-14	Si_diamond_A4	6.31E-05
Ti	8.51E-13	7.12E-16	Ti_bcc_A2	8.38E-02
V	1.14E-06	4.32E-09	V_bcc_A2	3.79E-01

Table F.4 – Activity and calculated activity coefficients of species in predicted end-phase austenite for MAG.

	austenite composition (FCC_A1#1) wt %	activity	reference phase	activity coefficient
Al	2.74E-11	2.70E-16	Al_liquid	9.84E-04
Ca	1.38E-20	3.52E-17	Ca_liquid	2.55E+05
Fe	99.999	0.99999	Fe_FCC_A1	1.00E+00
Mg	4.37E-15	1.26E-13	Mg_liquid	2.90E+03
Mn	2.61E-04	1.95E-06	Mn_cub_A13	7.47E-01
O	4.63E-09	1.01E-17	O2(g)	2.18E-07
P	1.01E-03	6.33E-10	P_liquid	6.24E-05
Si	2.56E-08	1.61E-14	Si_diamond_A4	6.26E-05
Ti	6.11E-13	5.09E-16	Ti_bcc_A2	8.34E-02
V	2.57E-06	9.69E-09	V_bcc_A2	3.77E-01